

# Negative spherical aberration ultrahigh-resolution imaging in corrected transmission electron microscopy

Knut W. Urban, Chun-Lin Jia, Lothar Houben, Markus Lentzen, Shao-Bo Mi and Karsten Tillmann

*Phil. Trans. R. Soc. A* 2009 **367**, 3735-3753  
doi: 10.1098/rsta.2009.0134

## Supplementary data

["Audio Supplement"](#)

<http://rsta.royalsocietypublishing.org/content/suppl/2009/08/11/367.1903.3735.DC1.html>

## References

[This article cites 37 articles, 3 of which can be accessed free](#)

<http://rsta.royalsocietypublishing.org/content/367/1903/3735.full.html#ref-list-1>

## Rapid response

[Respond to this article](#)

<http://rsta.royalsocietypublishing.org/letters/submit/roypta;367/1903/3735>

## Subject collections

Articles on similar topics can be found in the following collections

[electron microscopy](#) (16 articles)

## Email alerting service

Receive free email alerts when new articles cite this article - sign up in the box at the top right-hand corner of the article or click [here](#)

---

To subscribe to *Phil. Trans. R. Soc. A* go to:  
<http://rsta.royalsocietypublishing.org/subscriptions>

---

# Negative spherical aberration ultrahigh-resolution imaging in corrected transmission electron microscopy

BY KNUT W. URBAN\*, CHUN-LIN JIA, LOTHAR HOUBEN, MARKUS LENTZEN,  
SHAO-BO MI AND KARSTEN TILLMANN

*Institute of Solid State Research and Ernst Ruska Centre for Microscopy and  
Spectroscopy with Electrons, Research Centre Jülich, 52425 Jülich, Germany*

Aberration-corrected transmission electron microscopy allows us to image the structure of matter at genuine atomic resolution. A prominent role for the imaging of crystalline samples is played by the negative spherical aberration imaging (NCSI) technique. The physical background of this technique is reviewed. The especially high contrast observed under these conditions owes its origin to an enhancing combination of amplitude contrast due to electron diffraction channelling and phase contrast. A number of examples of the application of NCSI are reviewed in order to illustrate the applicability and the state-of-the-art of this technique.

**Keywords:** electron microscopy; aberration correction; contrast; ferroelectrics

## 1. Introduction

With the realization of the Rose corrector (Rose 1990; Haider *et al.* 1998; Uhlemann & Haider 1998), the old dream of electron optics to be able to construct spherical aberration-corrected lens systems has come true. Today, a new generation of commercial transmission electron microscopes is on the market making aberration-corrected high-resolution imaging available to a growing group of researchers, in particular, in materials science. The work that has been carried out using aberration-corrected electron microscopy in this field in the past 10 years has recently been reviewed (Urban 2008). With the extraordinary results presented therein, this study has demonstrated the potential of the new technology. On the other hand, it has also shown that the techniques which have to be applied to obtain optimum results are quite elaborate and are by far not routine. Interesting, also from a science-sociological point of view, is the fact that the general scientific community appears not to be prepared for the new qualities offered by aberration-corrected transmission electron microscopy.

\*Author for correspondence ([k.urban@fz-juelich.de](mailto:k.urban@fz-juelich.de)).

One contribution of 14 to a Discussion Meeting Issue ‘New possibilities with aberration-corrected electron microscopy’.

In particular, there are four facts that materials scientists outside the electron microscopy community should take note of. The *first* concerns the circumstance that now, for the first time, genuine atomic resolution is available. Not every ‘image’ published in the past that showed a grating of black or white dots was actually an atomic resolution image. In contrast to the bulk of the previous work, it is possible today not only to separate atomic columns (imaged end-on) from each other laterally, but also to measure the position of individual atom columns with a precision of up to about a hundredth of an atomic diameter and to determine the occupancy of a given column with atoms. This is equivalent to local concentration measurements on the atomic scale (Jia *et al.* 2003; Jia & Urban 2004; Houben *et al.* 2006). The *second* fact is that, in transmission electron microscopy, atomic structures are not imaged in a way comparable to that typical for microscopy in light optics where the information is largely obtained by exploiting the locally varying absorption of light in the sample. This erroneous view is surprisingly quite common, and it is at the origin of the problem that, quite frequently, electron microscopic results are not only underestimated in value, but also quite often misinterpreted. The atomic world is that of quantum mechanics, and in these dimensions, the term image loses its conventional meaning. Much of the contrast is ultimately based on quantum mechanical phase shifts experienced by the electron wave field by interaction with the interatomic potential. To deduce the atomic structure backward from images is, hence, a highly nonlinear problem that is not easy to solve. In general, this includes at least two steps: (i) to retrieve the electron wave function at the exit plane (EPWF) of the specimen and (ii) to find an atomic model for which, taking into account the sample parameters (in particular thickness and crystallographic orientation) and the imaging conditions, quantum mechanics yields an EPWF matching the experimental one (e.g. Stadelmann 1987; Tillmann, *et al.* 2004; Urban *et al.* 2008). The *third* fact is that, again in contrast to light microscopy in which total elimination of aberrations is the standard in precision optics, imaging in the fully spherical aberration-corrected mode, although technically feasible, is never used. In order to get access to the quantum mechanical phase shifts of the electron wave function, a certain, well-defined amount of residual spherical aberration has to be adjusted, on purpose, to optimize contrast. Finally, the general physics community should take note that there is a basic difference between *resolution* (in general defined by the Rayleigh criterion) and *precision*. Although this is the subject of undergraduate courses in optics, it appears difficult to accept that the new electron microscopes offering a Rayleigh resolution of 0.08 nm allow atomic shifts as small as a few picometres to be measured reliably, which is by more than an order of magnitude better (den Dekker *et al.* 1999, 2005; Van Aert *et al.* 2005; Houben *et al.* 2006). Actually, it is this extremely high precision of atomic position measurements that provides materials science with extraordinary new opportunities (Jia *et al.* 2008).

In this contribution, we shall discuss some of the above issues briefly, as far as this is feasible, taking into account space limitations. On the other hand, this discussion provides the background for the treatment of the negative spherical aberration imaging (NCSI) mode that provides materials science with contrast surpassing that is offered by other conventional techniques. The NCSI mode is unique to aberration-corrected transmission electron microscopy and cannot be realized in classical uncorrected instruments.

## 2. The principles of atomic resolution imaging

### (a) Resolution and point spread

We treat the case of a crystalline specimen. This is illuminated by an electron plane wave with an incident wave vector  $\mathbf{k}_0$ ,

$$\psi(\mathbf{r}) = \exp(2\pi i \mathbf{k}_0 \cdot \mathbf{r}). \quad (2.1)$$

On its way through the specimen, this wave field interacts with the interatomic potential  $V(\mathbf{r})$ . Taking into account the high electron energy of typically 200–300 keV, the electron wave function  $\psi(\mathbf{r})$  in the crystal represents a solution of the relativistic Dirac equation. In a small-angle scattering approximation, spin polarization can be neglected and the equation adopts a Schrödinger-type form with relativistically corrected mass and wavelength (Reimer 1984; Williams & Carter 1996; Spence 2007).

At the exit plane of the specimen, the interior wave field decomposes into a superposition of plane waves. This electron EPWF is, for simplicity, written as a Fourier integral,

$$\psi(\mathbf{r}) = \int_{\mathbf{g}} \psi(\mathbf{g}) \exp(2\pi i \mathbf{g} \cdot \mathbf{r}) d\mathbf{g}. \quad (2.2)$$

The individual components are characterized by the reciprocal vector  $\mathbf{g}$  representing the spatial frequency, with  $\mathbf{r}$  denoting the general position vector. The EPWF contains all the information on the specimen we can get; its elucidation is the object of the following optics. The wave field passes through the electromagnetic lens and we obtain an intensity distribution in the image plane given by the Poynting vector that, again in a small-angle approximation, is proportional to the probability density, i.e. the absolute square of the wave function,

$$I(\mathbf{r}) \propto \frac{i\hbar}{4\pi m} (\psi \nabla \psi^* - \psi^* \nabla \psi) \propto \psi^* \psi, \quad (2.3)$$

where  $\hbar$  is Planck's constant and  $m$  is the electron mass.

If the lens shows aberrations, these have the effect that the individual components  $\psi(\mathbf{g})$  of the EPWF are to be multiplied by the phase factor

$$\exp(-2\pi i \chi(\mathbf{g})), \quad (2.4)$$

where

$$\chi(\mathbf{g}) = \frac{1}{4} C_s \lambda^3 g^4 + \frac{1}{2} Z \lambda g^2 + \dots \quad (2.5)$$

is the wave-aberration function. It is approximated here by writing it in two terms. In modern ultrahigh-resolution studies, up to 14 terms have to be considered (Uhlemann & Haider 1998; Saxton 2000; Lentzen 2006). The first is due to spherical aberration, with  $C_s$  and  $\lambda$  representing the spherical aberration parameter and the electron wave length, respectively. The second term is the lens defocus contribution, with  $Z$  denoting the defocus parameter.

The result is then an aberration-modified wave function giving rise to a correspondingly modified intensity distribution in the image plane. The presence of aberrations has the consequence that a point in the object plane is not imaged

into a sharp point in the image plane, but rather into an error or point spread disc whose radius is given by the point spread function,

$$R = \max \left| \frac{\partial \chi}{\partial g} \right| = \max |C_s \lambda^3 g^3 + Z \lambda g + \dots|, \quad (2.6)$$

where the maximum has to be taken over the whole range of spatial frequencies contributing to the image (Reimer 1984; Lichte 1991).

It is obvious that, if the aberration function, as a result of perfect aberration correction, adopts the value zero, point spread vanishes, which is formally (neglecting other resolution-limiting effects) identical to the description that one obtains for an ideal Gaussian image of arbitrarily high resolution. However, resolution is only a necessary but not sufficient condition. Imaging also requires contrast.

### (b) Contrast

On the one hand, with the fast computers available today, it is not a problem to plug a certain potential  $V(\mathbf{r})$ , together with the specimen thickness, the imaging conditions and the lens properties into one of the various available computer codes to calculate the image intensity distribution. This fully dynamical image simulation is standard in today's practical high-resolution imaging (all the computed images shown in the following are obtained this way). On the other hand, in order to get insight into particular features of the image formation, it is common practice to treat special cases. First, for all realistic specimen thicknesses employed in transmission electron microscopy, a reduction in the total integrated intensity, corresponding to actual losses of electrons inside the specimen by particle absorption, can be excluded. In the following, we treat the two types of contrast, amplitude and phase contrast, separately. This is for clarity only, as, in general, both occur together in a convoluted manner.

We start the discussion, as usual, with phase contrast. This means that access to the specimen structure is obtained by exploiting the information contained in the locally varying phase of the EPWF. The underlying phase shift is introduced by the interaction of the wave field with the interatomic potential. In a more intuitive description, the atoms, owing to their electric field, are acting as regions of different refractive index. As in light microscopy under phase contrast conditions (Zernike 1942*a,b*), the problem arises that the atomic phase contrast has to be converted into visible amplitude contrast. In light microscopy, the phase shifts are small, whereas the phase shifts in electron microscopy, depending on the atomic number and the specimen thickness, can be quite large. Nevertheless, for simplicity, the weak phase object (WPO) approximation is generally applied (e.g. Reimer 1984; Williams & Carter 1996; Spence 2007). Schematically, the conditions can be illustrated in the Gaussian complex number plane (figure 1*a*). The incident wave is characterized by an arrow along the real axis. The diffracted wave is characterized by a vector along the imaginary axis, which takes account of the fact that the basic phase shift of a diffracted wave is  $\pi/2$  with respect to the incident wave. The sum of both results is a vector rotated in the mathematically positive direction by a small angle, but of essentially the same amplitude as that of the incident wave. By means of the Zernike technique in light microscopy, an additional  $\pi/2$  phase shift is imposed on the scattered

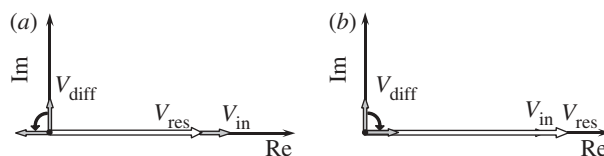


Figure 1. Amplitudes and phases in the Gaussian complex-number plane illustrating phase contrast in a WPO. The vector of the incident wave  $V_{\text{in}}$  is pointing along the *real* axis and that of the scattered wave  $V_{\text{diff}}$  along the *imaginary* axis. The basic phase shift of the diffracted wave is  $+\pi/2$ . (a) In the Zernike technique (Zernike 1942*a,b*) for positive phase contrast, an additional  $+\pi/2$  phase shift is applied to the diffracted wave. The vector sum  $V_{\text{res}}$  yields a vector with reduced modulus. In electron microscopy, atom positions appear dark on a bright background. (b) For negative phase contrast, the corresponding additional phase shift is  $-\pi/2$ . Atom positions appear bright on dark background. In conventional transmission electron microscopy, only (a) is feasible. Case (b) applies to NCSI conditions in an aberration-corrected instrument.

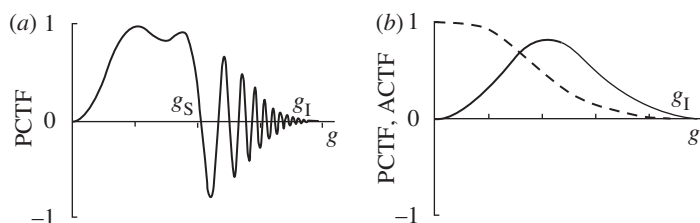


Figure 2. The value of the PCTF as a function of spatial frequency  $g$ . (a) Plot of  $-\sin 2\pi\chi(g)$  for an uncorrected microscope.  $\chi(g)$  is the wave aberration function according to equation (2.5). According to Scherzer (1949), the modulus is close to 1 for a range of  $g$  up to  $g_S$ , i.e. the Scherzer point resolution limit. (b) Plot of  $\sin 2\pi\chi(g)$  (solid line) for NCSI conditions in the aberration-corrected instrument (Lentzen 2004); the region of optimized contrast expands up to the information limit  $g_I$ . The amplitude contrast transfer function (ACTF)  $\cos 2\pi\chi(g)$  is also given (dashed line).

wave by the so-called  $\lambda/4$  plate. Now, summing up yields a substantially shorter resulting vector and a corresponding intensity reduction in the image. As a result, the scattering regions give a dark contrast on bright background. This is called *positive* phase contrast.

In spite of some progress, Zernike-type  $\lambda/4$  phase shifters are not yet available in electron microscopy. Following Scherzer (1949), the spatial frequency-dependent phase-shifting qualities of the lens aberration function (equation (2.5)) are exploited to bring about the quested contrast. According to Scherzer (1949), contrast is proportional to  $\sin 2\pi\chi(g)$ . The corresponding optimized phase contrast transfer function (PCTF) is displayed in figure 2*a* for an uncorrected instrument. Since the impact of aberrations has to be used to induce contrast, the latter is obtained at the expense of an increase in point spread (equation (2.6)). In colloquial language, one would say that the cost for obtaining contrast is that the image becomes unsharp to a certain extent. The corresponding PCTF for an aberration-corrected instrument, still maintaining the WPO approximation, was derived by Lentzen *et al.* (2002). While in Scherzer's original treatment, where the only variable one can dispose of is the lens defocus  $Z$ , aberration correction offers an additional degree of freedom, the spherical aberration parameter  $C_s$ .

Table 1. Typical optimum values for the spherical aberration parameter  $C_{s,\text{opt}}$ , the defocus parameter  $Z_{\text{opt}}$ , the radius of the point spread function  $R_{\text{opt}}$ , calculated by employing equations (2.7) to (2.9) and the respective values  $g_{\text{I}}$  for the information limit of 200 and 300 keV instruments.

$e$ , energy (keV)	$g_{\text{I}}^{-1}$ (nm)	$C_{s,\text{opt}}$ ( $\mu\text{m}$ )	$Z_{\text{opt}}$ (nm)	$R_{\text{opt}}$ (nm)
200	0.12	31	−10	0.07
300	0.07	7.5	−4.5	0.04
300	0.05	1.9	−2.3	0.03

This means that, against intuition, it is not meaningful to compensate spherical aberration entirely to zero, but to adjust the instrument for a defined amount of residual aberration. Together with the defocus parameter, this allows us to further optimize conditions compared with Scherzer's theory. In fact, one can minimize point spread, reduce the low-contrast (poor transfer) region at small spatial frequencies and eliminate the contrast oscillations between  $g_{\text{S}}$  and  $g_{\text{I}}$ . Here,  $g_{\text{S}}$  is the spatial frequency corresponding to Scherzer's point resolution and  $g_{\text{I}}$  denotes the spatial frequency marking the information limit determined by partial temporal coherence. This, in turn, is limited by the energy spread of the electron source and by fluctuations of the electron energy and the objective lens current (Hanszen & Trepte 1971; Reimer 1984; Barthel & Thust 2008). The optimum settings for phase contrast in an aberration-corrected instrument are

$$C_{s,\text{opt}} = +\frac{64}{27}(\lambda^3 g_{\text{I}}^4)^{-1}, \quad (2.7)$$

$$Z_{\text{opt}} = -\frac{16}{9}(\lambda g_{\text{I}}^2)^{-1} \quad (2.8)$$

and 
$$R_{\text{opt}} = \frac{16}{27}g_{\text{I}}^{-1}. \quad (2.9)$$

The corresponding PCTF is shown in figure 2*b*. Typical values for  $C_{s,\text{opt}}$ ,  $Z_{\text{opt}}$  and  $R_{\text{opt}}$  are given in table 1. With typical values of 0.5–1.2 mm for  $C_{\text{s}}$  in an uncorrected instrument, it is evident that the residual value required for contrast is only a few per cent of the original value of the spherical aberration parameter. A corresponding treatment including variable higher-order aberrations is given in Lentzen (2008).

### 3. Imaging under negative spherical aberration imaging conditions

#### (*a*) Enhanced contrast for imaging under negative spherical aberration conditions

So far, the treatment of Lentzen *et al.* (2002) is still conservative with respect to the direction of the Zernike phase shift adjusted to induce contrast. This means that, according to equations (2.7) and (2.8), positive phase contrast is obtained by which atomic positions appear dark on a bright background.

In early 2001, C.-L. Jia (2001, unpublished data) observed for the first time extraordinarily high contrast in  $\text{SrTiO}_3$ , with atomic positions appearing bright on dark background for certain settings of the electron microscope's aberration



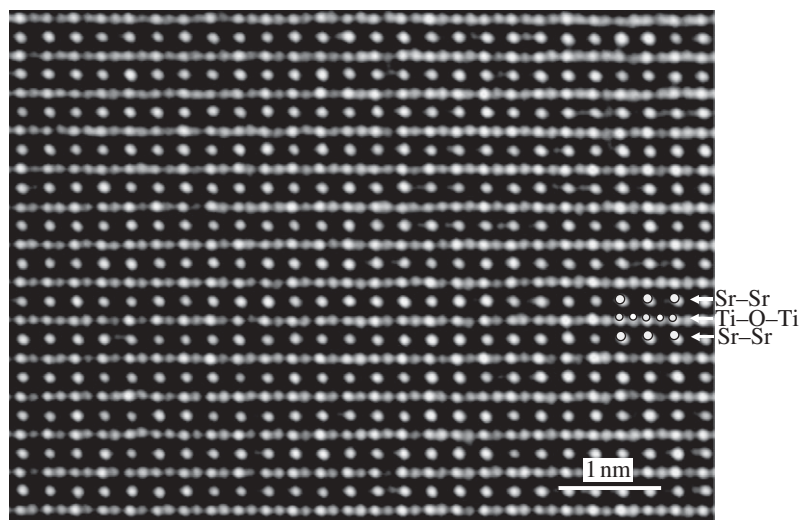


Figure 3. Experimental image of  $\text{SrTiO}_3$  taken along the  $[1\ 1\ 0]$  zone axis. All three atomic species are visible (see inset).

corrector. This observation was reported in the Materials Research Society Spring Meeting in San Francisco in April 2001 (K. W. Urban & C.-L. Jia 2001, unpublished data; see also fig. 7.2 in Spence (2007)). Shortly afterwards, it was shown by C.-L. Jia (2001, unpublished data) by means of image simulations that the contrast of these images, according to the definition ‘negative phase contrast’, is due to an overcompensation of spherical aberration of the objective lens, i.e. the contrast is due to imaging under negative spherical aberration conditions. Such a type of imaging mode had neither been used before nor had it been predicted or treated theoretically.

Figure 3 shows an experimental image of  $\text{SrTiO}_3$ . All atomic positions are visible (first prerequisite of full atomic resolution), including oxygen. Before, oxygen could never be seen directly in electron microscopic images. It was only accessible (Coene *et al.* 1991; Jia & Thust 1999; Kisielowski *et al.* 2001) via the EPWF reconstruction technique based on the exploitation of the information content of a series of about 20 images taken under different defocus conditions. Figure 4*a–c* shows simulated images for  $C_s = 0\ \mu\text{m}$ ,  $+40\ \mu\text{m}$  and  $-40\ \mu\text{m}$  for different defocus values and sample thicknesses at an electron energy of 200 keV. Figure 4*d* shows a direct comparison of the situation for positive  $C_s$ , combined with the usual underfocus (negative values of  $Z$ ), and of that for negative  $C_s$  and overfocus (positive values of  $Z$ ). Oxygen can definitely not be imaged at all parameter settings for positive phase contrast. This means that positive phase contrast does not supply us with full atomic details, in spite of the fact that the corrected optics is clearly sufficient to resolve the oxygen–titanium atom separation of 0.138 nm.

The enhanced contrast under negative spherical aberration imaging conditions compared with the corresponding positive spherical aberration conditions (figure 4*d*) is obvious. In order to get away from the ‘positive’ or ‘negative’



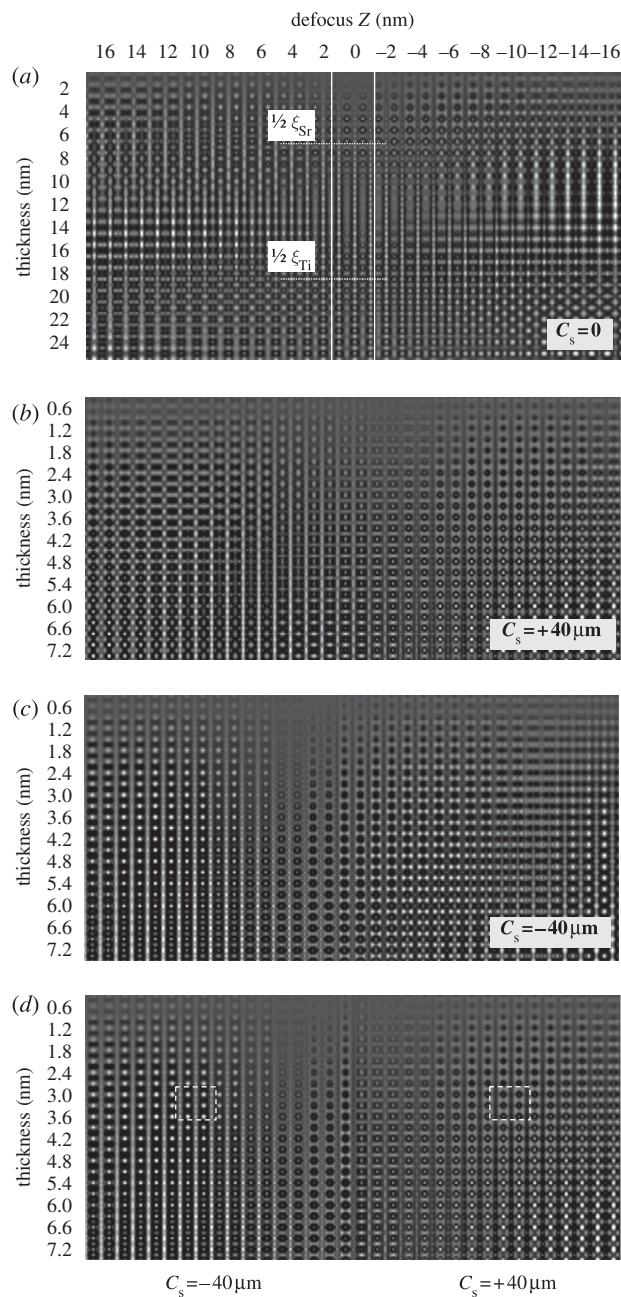


Figure 4. (a–c) Simulated images for  $C_s = 0 \mu\text{m}$ ,  $+40 \mu\text{m}$  and  $-40 \mu\text{m}$ , respectively, for different defocus values  $Z$  and sample thicknesses at an electron energy of 200 keV. (d) A direct comparison of the positive and negative  $C_s$  situation in which, in the  $-C_s$  case, overfocus (positive values of  $Z$ ) and, in the positive  $C_s$  case, the usual underfocus (negative values of  $Z$ ) is applied. The frame is used as a guide for the eye for same sample thickness.

phase contrast terminology (for the background of this terminology, e.g. see Williams & Carter 1996), we use for this new technique the term ‘negative spherical aberration imaging’.

(b) *The origin of contrast enhancement under negative spherical aberration imaging conditions*

First results employing the NCSI technique were published by Jia *et al.* (2003). This was followed by a more elaborated treatment of the physical background by Jia *et al.* (2004). Within the framework of the linear treatment of contrast for a WPO (Lentzen *et al.* 2002), inverting the sign of  $C_{s,\text{opt}}$  changes the positive to negative phase contrast, but does not yield any contrast enhancement. This can be concluded by comparison of figure 4*b* with figure 4*c* for rather small specimen thicknesses, for which the WPO approximation can be considered adequate. This situation corresponds to figure 1*b*. The vector for the diffracted wave is now tilted clockwise, i.e. in the mathematically negative sense, leading to enhanced intensity at scattering positions.

In order to arrive at an understanding of the contrast enhancement under NCSI conditions, two assumptions of the classical contrast theory of Scherzer (1949) have to be abandoned. The first is the WPO approximation. From figure 4, we can easily recognize that, at realistic sample thicknesses (approx. 1–10 nm), the WPO is inadequate and only a fully dynamical treatment of the electron scattering and imaging problem can give us an adequate description. The second is an approximation not yet discussed and this is the weak amplitude object (WAO) approximation (compare the treatment in Reimer (1984)).

If the specimen has an amplitude structure leading to a locally varying amplitude of the electron EPWF, amplitude contrast occurs. As we shall see below, such amplitude structure can occur owing to the quantum mechanics inside the specimen, even in cases in which classical electron absorption by matter can be neglected. In the linear theory (Scherzer 1949), the resulting amplitude contrast is proportional to  $\cos 2\pi\chi(\mathbf{g})$ . Ideally, in the case of  $\chi(\mathbf{g}) = 0$ , i.e. full compensation of spherical aberration and zero defocus, no phase contrast but optimum amplitude contrast is expected. The transfer function for amplitude contrast for NCSI conditions is displayed schematically in figure 2*b*.

By inspection of the centre of figure 4*a*,  $C_s = 0$  and  $Z = 0$ , we recognize that there is essentially no contrast at all at very low specimen thickness, where the WAO approximation is fulfilled best. Since, under these conditions, amplitude contrast, if there is any at all, should be seen best; we can conclude that there is no amplitude structure taking effect at these thicknesses. However, the situation changes at larger sample thicknesses. Under these conditions, neither the WPO nor the WAO is justified. Therefore, a discussion in which amplitude and phase contrast contributions are treated separately can only be qualitative at best. Of some help for this can be to neglect phase contrast and to carry out a Bloch wave calculation for estimating the local variation in the electron current density at the exit plane of the specimen. This approach is taken in the treatment of electron diffraction channelling (Howie 1966; Urban & Yoshida 1979; Van Dyck & Op de Beeck 1996). As has been discussed (e.g. Van Dyck & Op de Beeck 1996) for many cases, the situation is quite well described by treating the individual atomic columns independently. This allows us to calculate

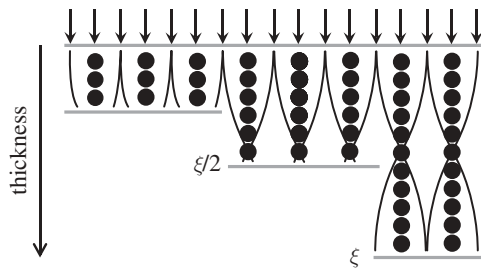


Figure 5. Schematic illustrating the effect of electron diffraction channelling on the local electron current density distribution for three different sample thicknesses. At the sample entrance surface, the electron current density distribution is assumed to be laterally uniform. The atom rows (respectively the interatomic potential) ‘focus’ the electrons towards the atomic strings. This leads to enhanced current density at the atom positions with the maximum at a depth of  $\xi/2$ , where  $\xi$  is the extinction distance, at the expense of that in between the atoms. This induces an amplitude structure of the sample. At large sample thicknesses, the current density at the atom positions decreases again and ideally the current density becomes uniform again at depth  $\xi$ . Note that the extinction distance depends on the atomic species forming the atom string.

the steady electron states in the transverse potential of the atomic string. The result of electron diffraction channelling is, phenomenologically, an oscillatory motion of the electrons, as schematically depicted in [figure 5](#) for three different sample thicknesses. This can be understood quite easily. At the specimen entrance surface, the electrons are equally distributed and the electron current density is uniform. While the electron wave penetrates into the specimen, an atomic string with a positive charge is acting on the electrons, attractively concentrating the electrons, like an electrostatic lens, on the atom positions after some distance from the entrance surface. Subsequently, the electrons fan out again, yielding an electron current density distribution after a certain distance that is the same as it was at the surface.

In the Bloch wave formalism, it is straightforward to calculate the extinction distance,

$$\xi = (k^{(i)} - k^{(j)})^{-1}, \quad (3.1)$$

where  $k^{(i)}$  and  $k^{(j)}$  denote the eigenvalues of the two most excited Bloch states ([Reimer 1984](#)). Solving numerically the corresponding eigenvalue problem, we find  $\xi_{\text{Sr}} \approx 14$  nm for an Sr atom column,  $\xi_{\text{Ti}} \approx 38$  nm for a Ti column and an even larger value for oxygen columns. Comparing this result with the atom column intensities in [figure 4a](#) (centre), we find that the atom positions appear brightest at depths of odd multiples of half the extinction distance, i.e. 7 nm for Sr and 19 nm for Ti. At larger depths, the contrast decreases again. This means that, at  $C_s = 0$  and  $Z = 0$ , the contrast is essentially determined by electron diffraction channelling-induced amplitude contrast ([Lentzen 2004](#)). Or, in more classical terms, the specimen exhibits a thickness-dependent ‘amplitude structure’, giving rise to corresponding amplitude contrast if the sample thickness is in a suitable range.

Now let us focus on [figure 4d](#). We find that, even when amplitude as well as phase contrast determine the image intensity distribution, we can recognize the effect of electron diffraction channelling. At moderate thicknesses, around 3 nm

(framed in the figure), the intensity at the Ti and O positions is still increasing, while that at Sr positions adopts a maximum. We note that, in between the atom positions, the intensity drops to very low values, which can be explained by the fact that, owing to the concentration of the electrons towards the atomic strings, the electron density is enhanced at these positions at the expense of that in between these strings.

Now it becomes evident that the strong contrast under NCSI conditions is due to *additive* contributions of both amplitude and phase contrast. On the one hand, the amplitude contrast increases, at moderate specimen thicknesses, at the atom positions. The negative phase contrast, leading to bright atom contrast at these positions, enhances the signal strength at the atom positions. On the other hand, the diffraction channelling effect reduces the electron density in between the atom positions. In this way, the contrast is enhanced.

We note that the contrast conditions are rather robust with respect to a variation in defocus and specimen thickness. In figure 4*d*, overfocus values of 6–13 nm and thickness values between 1.5 and 7 nm clearly show that the NCSI contrast allows us to image oxygen and thus to obtain full atomic resolution, which otherwise cannot be obtained directly. We also note that the adjusted value of  $C_s$  can vary over a wide range. Even a deviation of 30 per cent of the calculated optimum value does not destroy the high-resolution contrast, although it certainly changes the absolute contrast behaviour. The robustness of the bright-atom contrast conditions with respect to variations in defocus, spherical aberration and specimen thickness can be well explained by the tolerance limits for the respective aberration setting (Uhlemann & Haider 1998; Jia *et al.* 2004) and by the weak phase-variation of the scattered wave in a two-level channelling model of electron diffraction (Lentzen 2004). Therefore, we conclude that, in order to exploit the opportunities for direct atomic imaging offered by spherical aberration-corrected electron microscopy in crystalline specimens, NCSI conditions should be employed. Although the absolute values of  $C_s$  and of the other imaging parameters are important for quantitative contrast evaluation, this imaging mode *per se* does not make high demands with respect to the adjustment of particular values of these parameters.

*(c) Supporting arguments for the background of negative spherical aberration imaging*

The reader is reminded that the aforementioned arguments are based on a discussion in which a complicated dynamical scattering situation is substantially simplified to elucidate certain aspects of contrast formation. However, the details can only be explored by the numerical solution of the complete quantum mechanical and optical problem whose results are given in figure 4. However, the possibilities for an intuitive understanding of these results are rather limited as the intricate phase relations of the constituents of the electron wave field do not lend themselves to a simple interpretation. Two more issues appear to be useful for a more intuitive understanding of the background of NCSI conditions.

Jia *et al.* (2004) have studied the effect of linear imaging on NCSI. Their numerical simulations show that neglecting the cross terms in the calculation of the image intensity (typical for the WPO and WAO approximation) destroys the

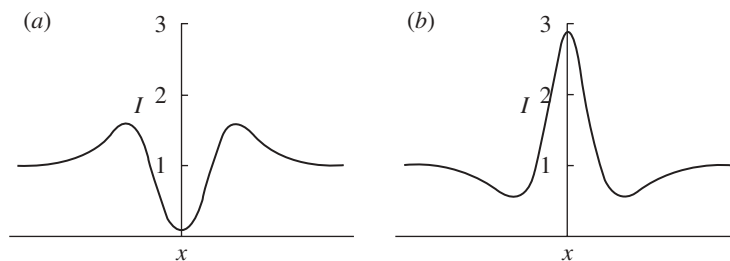


Figure 6. Illustration of the additive and subtractive contribution of the nonlinear term in equation (3.5) to the contrast at an atomic position. Intensity traces  $I(x)$  across atomic positions: (a) conventional case of 'positive' phase contrast with atoms appearing dark on a bright background and (b) NCSI conditions yield bright, i.e. negative, phase contrast on a dark background. The nonlinear term takes account of the diffraction channelling effect depicted in figure 5, enhancing contrast.

particular contrast enhancement. This clearly proves that NCSI is a technique particularly suited for material research samples of realistic thicknesses, which are, apart from special cases, not 'weak' in the sense of linear contrast theory.

The second issue concerns an intuitive argument originally suggested by A. Thust (2004, unpublished data) and described by Jia *et al.* (2004). A simple picture can be gained if an ideal Zernike phase plate is assumed for both imaging modes (Jia *et al.* 2004), that is, transmission of the direct, unscattered wave  $\psi_0$  with a coefficient of 1 and transmission of the scattered wave,

$$\psi_{\text{sc}}(\mathbf{r}) = \pi i \lambda U(\mathbf{r}) t, \quad (3.2)$$

where  $U(\mathbf{r})$  denotes the projected crystal potential and  $t$  is the specimen thickness. The exit wave in the object plane,

$$\psi_{\text{obj}}(\mathbf{r}) = \psi_0 + \pi i \lambda U(\mathbf{r}) t, \quad (3.3)$$

is altered by the phase plate to the exit wave in the imaging plane,

$$\psi_{\text{im}}(\mathbf{r}) = \psi_0 \mp \pi \lambda U(\mathbf{r}) t, \quad (3.4)$$

with a coefficient of  $+i$  for positive phase contrast and  $-i$  for negative phase contrast. The resulting image intensity to second order in  $U(\mathbf{r})$  is

$$I(\mathbf{r}) = \psi_0^2 \mp 2\pi \psi_0 \lambda U(\mathbf{r}) t + (\pi \lambda U(\mathbf{r}) t)^2. \quad (3.5)$$

The upper sign holds for positive phase contrast and the lower sign for negative phase contrast, and a common phase of  $\psi_0$  and  $\psi_{\text{sc}}(\mathbf{r})$  has been chosen to set  $\psi_0$  to a real value. Figure 6 displays the intensity traces across an atom column site. The comparison of these two cases shows that the linear contribution and the quadratic contribution have a different sign for positive phase contrast. On the one hand, the local intensity modulation at an atom column site becomes weak because the linear modulation (second term in equation (3.5)) is partially cancelled by the nonlinear modulation (third term). On the other hand, the linear contribution and the quadratic contribution have the same sign for negative phase contrast. As a consequence, the local intensity modulation at an atom column site is strong because linear and nonlinear modulations reinforce each other. In other words, setting up a negative spherical aberration combined with an overfocus



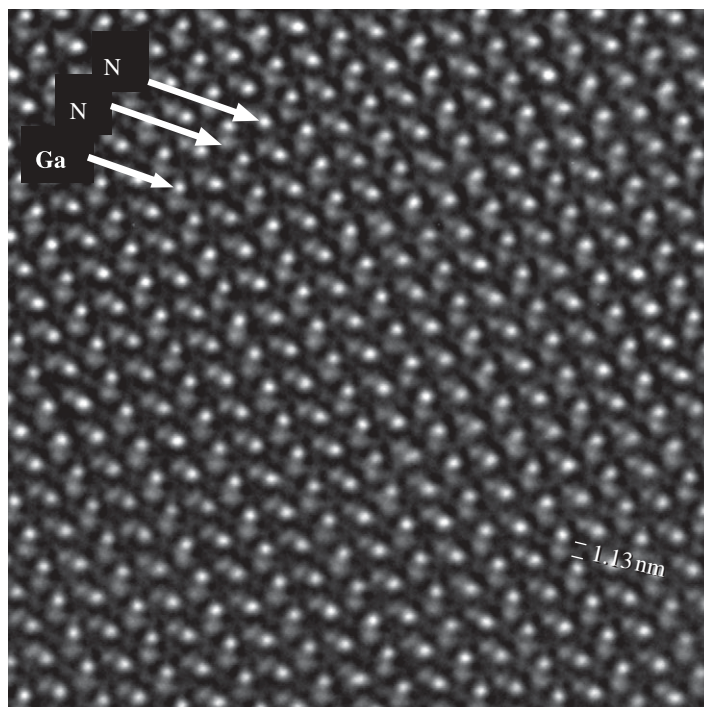


Figure 7. NCSI image of GaN. The Ga atom positions and the two types of nitrogen positions (N) are indicated.

enhances the atomic contrast compared with a setting with positive spherical aberration and underfocus. The above argument holds for ‘not so weak’ objects where, in contrast to the case of ‘weak’ objects (where the second-order term is neglected), terms up to second order are maintained in equation (3.5).

#### 4. Examples of the application of negative spherical aberration imaging to materials problems

##### (a) *Illustrative examples in materials science and solid-state chemistry*

In order to illustrate the general applicability of this new technique. Figures 7–10 display four additional cases of experimental NCSI imaging, in GaN, at an Si/SrTiO<sub>3</sub> interface (Mi *et al.* 2008), in the incommensurate misfit layer compound (PbS)<sub>1.14</sub>NbS<sub>2</sub> (Garbrecht *et al.* 2008) and in ZnO doped with In<sub>2</sub>O<sub>3</sub> (Svete *et al.* 2007). Also in other compounds, composed of high-nuclear charge with low-nuclear charge atom species, science has been ‘blind’ so far with regard to imaging the latter. Besides the oxides another example is GaN. As demonstrated by figure 7, full atomic resolution, including the imaging of nitrogen, is now available. At the Si/SrTiO<sub>3</sub> interface (figure 8), a monolayer of SrO faces the terminating plane of silicon. The strontium atoms are located above the face centre of four silicon atoms in the terminating plane, and the oxygen atoms are located directly above the terminating silicon atoms. According

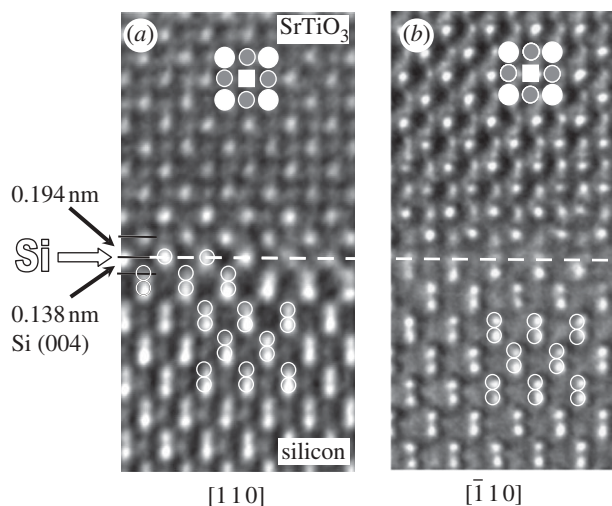


Figure 8. Si/SrTiO<sub>3</sub> interface in: (a) [110] and (b)  $\bar{1}10$  projection. In SrTiO<sub>3</sub>, all the atomic species, Ti (squares), Sr (white filled circles) and O (black filled circles) can be seen. The last Si atom (open circles) layer can be inferred from a measurement of the vertical lattice row separations (Mi *et al.* 2008). Note that the images show some contrast artefacts in the weak intensity background. These result from the low transfer of low-spatial frequency information expressed by the particular shape of the PCTF of figure 2b. The particular transfer properties and their effect on the resulting images are discussed by Lentzen (2004) and Tillmann *et al.* (2004).

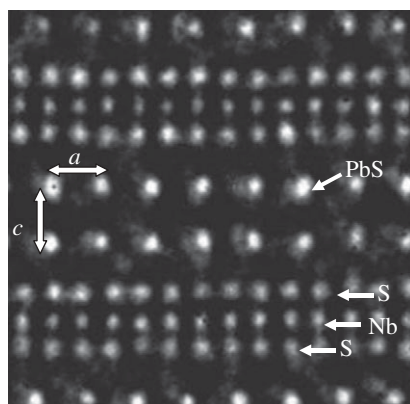


Figure 9. Incommensurate misfit layer compound (PbS)<sub>1.14</sub>NbS<sub>2</sub>. The individual atomic species are indicated. As inferred from a Gaussian regression analysis, the horizontal atom pair separation  $a = 0.286$  nm and, according to a Gaussian regression analysis, the vertical atom separation  $c = 0.314$  nm can be measured at a precision of  $\pm 6$  pm (Garbrecht *et al.* 2008).

to first-principles calculations, this interface structure, not observed before, has particularly low energy (Zhang *et al.* 2003). This study is a particular illustrative example for the new qualities of the work that is now possible at full atomic resolution. In fact, the structure of the Si/SrTiO<sub>3</sub> interface has, in search of interfaces with technically important high band offsets, been the



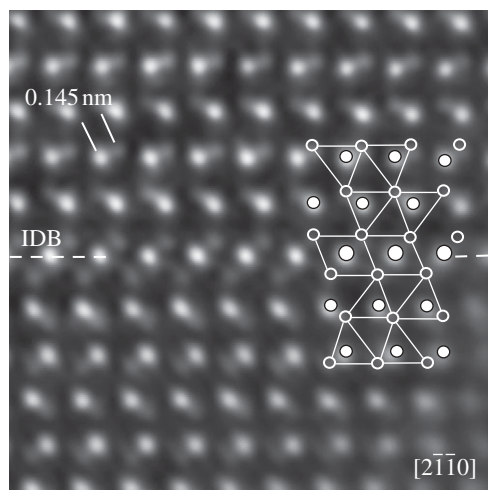


Figure 10. NCSI image of ZnO doped with  $\text{In}_2\text{O}_3$  showing (inclined broken line) an IDB on the basal plane of ZnO. The positions of all atomic columns can be identified (small filled circles denote zinc and empty circles denote oxygen). The ball and stick model indicates the coordination polyhedra. The In atoms (large filled circles) substitute for Zn on the IDB plane (Svete *et al.* 2007).

subject of numerous theoretical treatments. However, the limited resolution of the earlier experimental work and the problems arising from the fact that oxygen could not be imaged so far did not allow us to distinguish between the different structural models suggested. High-resolution electron microscopy of  $(\text{PbS})_{1.14}\text{NbS}_2$  is particularly challenging because of special structural features associated with this incommensurate misfit layer compound. The layer interfaces are incommensurate in one in-plane direction because of the different periodicities of the adjacent lattices. Also, light (S) and heavy atom columns (alternating Pb and S) occupy opposite positions at each interface. Garbrecht *et al.* (2008) showed that imaging of the complete projected crystal structure, including atomic column positions at the interfaces, becomes only possible by applying NCSI conditions (figure 9). Further investigations revealed that interface phenomena, such as inhomogeneities, layer distortions and stacking disorder, which so far could only be investigated by spatially averaging X-ray diffraction techniques, can now be quantitatively analysed on a local scale. The NCSI image of ZnO doped with  $\text{In}_2\text{O}_3$  shows an inversion domain boundary (IDB) parallel to the basal plane of ZnO (figure 10). The positions of all atomic columns can be accessed, and coordination polyhedra can be drawn in. The IDB is characterized by a closely packed indium layer, and the octahedral coordination of indium by oxygen can be deduced (Svete *et al.* 2007).

#### (b) Measuring ferroelectric domain walls in PZT

PZT, which stands for  $\text{Pb}(\text{Zr}_{0.2}\text{Ti}_{0.8})\text{O}_3$ , is a technical ferroelectric, widely used, for instance, in the form of thin films in ferroelectric memories. Data storage is performed by switching the ferroelectric polarization. The polarization state migrates through the specimen, and areas of different polarization are separated

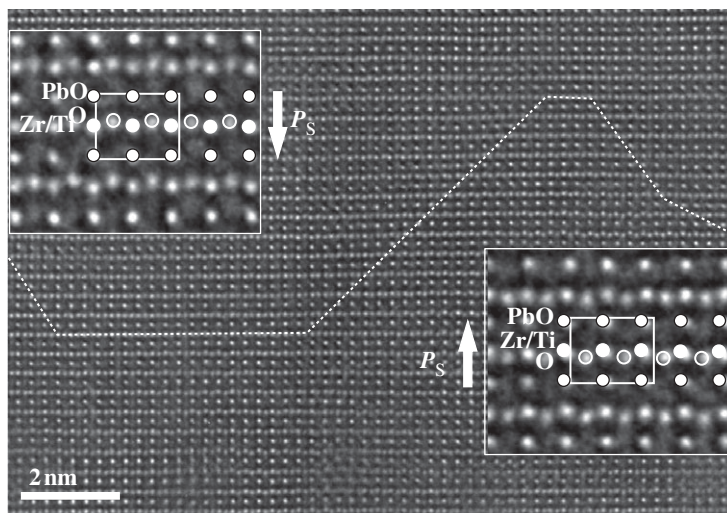


Figure 11.  $\text{Pb}(\text{Zr}_{0.2}\text{Ti}_{0.8})\text{O}_3$  imaged along the  $[1\ 1\ 0]$  direction. The inset on the left-hand side shows that the horizontal Zr/Ti atom rows are shifted towards the respective Pb atom row above the Zr/Ti row. O is shifted even more, thus becoming no longer collinear with the Zr/Ti rows. This indicates that the material is ferroelectrically polarized. The polarization vector  $\mathbf{P}_S$  is pointing downwards. The inset on the right-hand side shows opposite atomic shifts. The direction of the polarization vector is upward. The dotted line shows the appertaining ferroelectric inversion domain wall. With respect to the atomic structure, the inclined domain wall sections consist of vertical transversal and horizontal longitudinal domain wall segments. As a result, they are uncharged. The horizontal sections are longitudinal domain walls that are charged.

by domain walls in which the state of polarization changes from one direction to the other. So far, it was not possible to study these domain walls on an atomic scale owing to a lack of resolution.

Figure 11 displays a high-resolution electron micrograph taken under NCSI conditions (Jia *et al.* 2008). The insets are magnifications that allow us to identify the individual atomic species and to have a closer look at the particular position of the atomic sites. The individual atomic sites are indicated. Evidence for the polarized state can be obtained by inspection of the individual atomic sites in the unit cell. In the left-hand inset, the Zr/Ti (mixed) sites are shifted towards the upper vertical Pb atom row. The O atoms are shifted even further. As a result, they are no longer collinear with the Zr/Ti atom row. According to the definition, the polarization vector there is pointing downwards. In the inset on the lower right, the shifts are in the opposite direction and, as a consequence, the polarization vector is inverted. In between, we have a  $180^\circ$  inversion domain wall (broken line).

The oblique parts of the wall are made up of transversal segments and very short longitudinal segments. They are essentially uncharged since the electric fields characterized by the polarization vectors of the adjoining boundary segments just cancel each other. In the horizontal segments of the domain wall, the polarization vectors are, across the wall, meeting head-to-head. As a result, in the wall, the electric fields do not cancel and the boundary is charged. This is a surprising observation since, owing to their high field energy, longitudinal

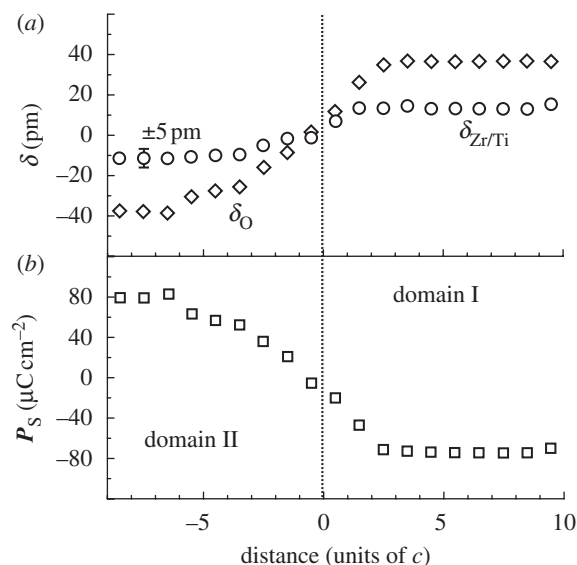


Figure 12. (a) Longitudinal inversion domain wall atom shifts measured on the atomic sites and averaged for better statistics.  $\delta_{\text{Zr/Ti}}$  denotes the upward shift of the Zr/Ti atom positions towards Pb (cf. left-hand inset in figure 11) as a function of distance (in units of the crystallographic  $c$  lattice parameter) from the domain wall centre.  $\delta_{\text{O}}$  denotes the corresponding oxygen atom shift. The domain wall width, amounting to 10 unit cell distances, is much wider than the transversal or mixed wall sections, which are only 1 projected unit cell in width. This allows the electric field energy to be reduced. (b) The macroscopic spontaneous polarization  $P_S$  obtained on the basis of measuring the individual atomic shifts (Jia *et al.* 2008).

domain walls were thought not to be able to exist. Since we have genuine atomic resolution, we have access to each individual atomic position in this  $\langle 110 \rangle$  projection. This allows us to make individual measurements of the atomic shifts.

Figure 12a shows, for a longitudinal domain wall, the results of the measurements of the atomic shifts of the O and Zr/Ti atoms out of their symmetry positions with single atom column resolution. The atomic separations were measured fitting two-dimensional Gaussians to the atomic intensity maxima (Houben *et al.* 2006). The Gaussian regression analysis indicates a precision of better than  $\pm 5 \text{ pm}$  (for a 95% confidence level). This wall is rather extended, about 10 lattice constants. From these measurements, we can infer that this kind of domain wall reduces the field energy by increasing its width substantially over that of the transversal wall whose width amounts only to about a single unit cell distance (Jia *et al.* 2008).

Figure 12b shows the value of the macroscopic spontaneous polarization  $P_S$  calculated from the measured atomic shifts, employing values for the effective charges of the ions given by Zhong *et al.* (1994). Indeed, exploiting the potential of the new ultrahigh-resolution techniques, we can determine local physical properties, for cases where these depend on structure and atomic displacements, directly from measurements of shifts of the individual atom positions. This fulfils an old dream in materials science to be able to obtain a direct link between atomic level information and macroscopic properties.

## References

- Barthel, J. & Thust, A. 2008 Quantification of the information limit of transmission electron microscopes. *Phys. Rev. Lett.* **101**, 200801-1–200801-4.
- Coene, W., Janssen, G., Op de Beeck, M. & Van Dyck, D. 1992 Phase retrieval through focus variation for ultra-resolution in field emission transmission electron microscopy. *Phys. Rev. Lett.* **69**, 3743–3746. (doi:10.1103/physRevLett.69.3743)
- den Dekker, A. J., Sijbers, J. & Van Dyck, D. 1999 How to optimize the design of a quantitative HREM experiment so as to attain the highest precision. *J. Microsc.* **194**, 95–104. (doi:10.1046/j.1365-2818.1999.00473.x)
- den Dekker, A. J., Van Aert, S., van den Bos, A. & Van Dyck, D. 2005 Maximum likelihood estimation of structure parameters from high resolution electron microscopy images. Part I: a theoretical framework. *Ultramicroscopy* **104**, 83–106. (doi:10.1016/j.ultramic.2005.03.001)
- Garbrecht, M., Spiecker, E., Jäger, W. & Tillmann, K. 2008 Quantitative electron microscopy for materials science. *Mat. Res. Soc. Symp. Proc.* **1026E**, C10–C11.
- Haider, M., Uhlemann, S., Schwan, E., Rose, H., Kabius, B. & Urban, K. 1998 Electron microscopy image enhanced. *Nature* **392**, 768–769. (doi:10.1038/33823)
- Hanszen, K.-J. & Treppe, L. 1971 The influence of voltage and current fluctuations and of a finite energy width of the electrons on contrast and resolution in electron microscopy. *Optik* **32**, 519–538.
- Houben, L., Thust, A. & Urban, K. 2006 Atomic-precision determination of the reconstruction of a 90° tilt boundary in YBa<sub>2</sub>Cu<sub>3</sub>O<sub>7</sub> by aberration corrected HRTEM. *Ultramicroscopy* **106**, 200–214. (doi:10.1016/j.ultramic.2005.07.009)
- Howie, A. 1966 Diffraction channelling of fast electrons and positrons in crystals. *Phil. Mag.* **14**, 223–237. (doi:10.1080/14786436608219008)
- Jia, C.-L. & Thust, A. 1999 Investigation of atom displacements at a  $\Sigma 3$  {111} twin boundary in BaTiO<sub>3</sub> by means of phase-retrieval electron microscopy. *Phys. Rev. Lett.* **82**, 5052–5055. (doi:10.1103/PhysRevLett.82.5052)
- Jia, C.-L. & Urban, K. 2004 Atomic-resolution measurement of oxygen concentration in oxide materials. *Science* **303**, 2001–2004. (doi:10.1126/science-1093617)
- Jia, C.-L., Lentzen, M. & Urban, K. 2003 Atomic-resolution imaging of oxygen in perovskite ceramics. *Science* **299**, 870–873. (doi:10.1126/science.1079121)
- Jia, C.-L., Lentzen, M. & Urban, K. 2004 High resolution transmission electron microscopy using negative spherical aberration. *Microsc. Microanal.* **10**, 174–184. (doi:10.1017/S1431927604040425)
- Jia, C.-L., Mi, S.-B., Urban, K., Vrejoiu, I., Alexe, M. & Hesse, D. 2008 Atomic-scale study of electric dipoles near charged and uncharged domain walls in ferroelectric films. *N. Mater.* **7**, 57–61. (doi:10.1038/nmat2080)
- Kisielowski, C., Hetherington, C. J. D., Wang, Y. C., Kilaas, R., O’Keefe, M. A. & Thust, A. 2001 Imaging columns of the light elements carbon, nitrogen and oxygen with sub Ångström resolution. *Ultramicroscopy* **89**, 243–263. (doi:10.1016/S0304-3991(01)00090-0)
- Lentzen, M. 2004 The tuning of a Zernike phase plate with defocus and variable spherical aberration and its use in HRTEM imaging. *Ultramicroscopy* **99**, 211–220. (doi:10.1016/j.ultramic.2003.12.007)
- Lentzen, M. 2006 Progress in aberration-corrected high-resolution transmission electron microscopy using hardware aberration correction. *Microsc. Microanal.* **12**, 191–205. (doi:10.1017/S1431927606060326)
- Lentzen, M. 2008 Contrast transfer and resolution limits for sub-Ångström high-resolution transmission electron microscopy. *Microsc. Microanal.* **14**, 16–26. (doi:10.1017/S1431927608080045)
- Lentzen, M., Jahnen, B., Jia, C.-L., Thust, A., Tillmann, K. & Urban, K. 2002 High-resolution imaging with an aberration corrected transmission electron microscope. *Ultramicroscopy* **92**, 233–242. (doi:10.1016/S0304-3991(02)00139-0)
- Lichte, H. 1991 Optimum focus for taking electron holograms. *Ultramicroscopy* **38**, 13–22. (doi:10.1016/0304-3991(91)90105-F)

- Mi, S.-B., Jia, C.-L., Vaithyanathan, V., Houben, L., Schubert, J., Schlom, D. G. & Urban, K. 2008 Atomic structure of the interface between SrTiO<sub>3</sub> thin films and Si (001) substrates. *Appl. Phys. Lett.* **93**, 101913-1–101913-3.
- Reimer, L. 1984 *Transmission electron microscopy*. Berlin, Germany: Springer.
- Rose, H. 1990 Outline of a spherically corrected semiaplanatic medium-voltage transmission electron microscope. *Optik* **85**, 19–24.
- Saxton, W. O. 2000 A new way of measuring microscope aberrations. *Ultramicroscopy* **81**, 41–45. (doi:10.1016/S0304-3991(99)00163-1)
- Scherzer, O. 1949 The theoretical resolution limit of the electron microscope. *J. Appl. Phys.* **20**, 20–29. (doi:10.1063/1.1698233)
- Spence, J. C. H. 2007 *High resolution electron microscopy*, 3rd edn. Oxford, UK: Oxford University Press.
- Stadelmann, P. A. 1987 EMS—a software package for electron diffraction analysis and HREM image simulation in materials science. *Ultramicroscopy* **21**, 131–145. (doi:10.1016/0304-3991(87)90080-5)
- Svete, M., Houben, L., Tillmann, K. & Mader, W. 2007 Imaging light atoms at sub-ångström resolution in an image side CS-corrected electron microscope FEI Titan 80-300. *Microsc. Microanal.* **13**(Suppl. 3), 30–31. (doi:10.1017/S1431927607080154)
- Tillmann, K., Thust, A. & Urban, K. 2004 Spherical aberration correction in tandem with exit-plane wave function reconstruction: interlocking tools for the atomic scale imaging of lattice defects in GaAs. *Microsc. Microanal.* **10**, 185–198. (doi:10.1017/S1431927604040395)
- Uhlemann, S. & Haider, M. 1998. Residual wave aberrations in the first spherical aberration corrected transmission electron microscope. *Ultramicroscopy* **72**, 109–119. (doi:10.1016/S0304-3991(97)00102-2)
- Urban, K. W. 2008 Studying atomic structures by aberration-corrected transmission electron microscopy. *Science* **321**, 506–510. (doi:10.1126/science/1152800)
- Urban, K. & Yoshida, N. 1979 The effect of electron diffraction channelling on the displacement of atoms in electron-irradiated crystals. *Radiat. Effects Defects Solids* **42**, 1–15. (doi:10.1080/10420157908201730)
- Urban, K. W., Houben, L., Jia, C.-L., Lentzen, M., Mi, S.-B., Tillmann, K. & Thust, A. 2008 Atomic-resolution aberration-corrected transmission electron microscopy. In *Advances in imaging and electron physics*, vol. 153 (ed. P. Hawkes), pp. 320–344. Oxford, UK: Academic Press.
- Van Aert, S., den Dekker, A. J., van den Bos, A., Van Dyck, D. & Chen, J. H. 2005 Maximum likelihood estimation of structure parameters from high resolution electron microscopy images. Part II: a practical example. *Ultramicroscopy* **104**, 107–125. (doi:10.1016/j.ultramic.2005.03.002)
- Van Dyck, D. & Op de Beeck, M. 1996 A simple intuitive theory for electron diffraction. *Ultramicroscopy* **64**, 199–207.
- Williams, D. B. & Carter, C. B. 1996 *Transmission electron microscopy*. New York, USA: Plenum Press.
- Zernike, F. 1942a Phase contrast, a new method for the microscopic observation of transparent objects, part I. *Physica* **9**, 686–698. (doi:10.1016/S0031-8914(42)80035-X)
- Zernike, F. 1942b Phase contrast, a new method for the microscopic observation of transparent objects, part II. *Physica* **9**, 974–986. (doi:10.1016/S0031-8914(42)80079-8)
- Zhang, X., Demkov, A. A., Li, H., Hu, X., Wie, Y. & Kulik, J. 2003 Atomic and electronic structure of the Si/SrTiO<sub>3</sub> interface. *Phys. Rev. B* **68**, 125323-1–125323-6.
- Zhong, W., King-Smith, R. D. & Vanderbilt, D. 1994 Giant LO–TO splittings in perovskite ferroelectrics. *Phys. Rev. Lett.* **72**, 3618–3621. (doi:10.1103/PhysRevLett.72.3618)